Negligible-Pb-Waste and Upscalable Perovskite Deposition Technology for High Operational-Stability Perovskite Solar Modules

Yan Jiang, Mikas Remeika, Zhanhao Hu, Emilio J. Juarez-Perez, Longbin Qiu, Zonghao Liu, Taehoon Kim, Luis K. Ono, Dae-Yong Son, Zafer Hawash, Matthew R. Leyden, Zhifang Wu, Lingqiang Meng, Jinsong Hu, and Yabing Qi*

Dr. Y, Jiang, Dr. M. Remeika, Dr. Z. Hu, Dr. E. J. Juarez-Perez, Dr. L. Qiu, Dr. Z. Liu, Dr. T. Kim, Dr. L. K. Ono, Dr. D. Son, Dr. Z. Hawash, Dr. M. R. Leyden, Dr. Z. Wu, Dr. L. Meng, Prof. Y. B. Qi
Energy Materials and Surface Sciences Unit (EMSSU) Okinawa Institute of Science and Technology Graduate University (OIST) 1919-1 Tancha, Onna-son, Kunigami-gun, Okinawa 904-0495, Japan
*E-mail: Yabing.Qi@OIST.jp
Prof. J. Hu
National Research Center for Molecular Sciences, Key Laboratory of Molecular Nanostructure and Nanotechnology, Institute of Chemistry, Chinese Academy of Sciences, Beijing 100190, P. R. China

Abstract:

We report an upscalable perovskite film deposition method combining raster ultrasonic spray (RUS) coating and chemical vapor deposition (CVD). Our method overcomes the coating size limitation of the existing stationary spray, single-pass spray and spin-coating methods. In contrast with the spin-coating method (>90% Pb waste), negligible Pb waste during PbI_2 deposition makes this method more environmentally friendly. Outstanding film uniformity across the entire area of 5 cm × 5 cm is confirmed by both large area compatible characterization methods (electroluminescence and scattered light imaging) and local characterization methods (AFM, SEM, photoluminescence mapping, UV-vis and XRD measurements on multiple sample locations), resulting in low solar cell performance decrease upon increasing device area. With the $FAPb(I_{0.85}Br_{0.15})_3$ perovskite layer deposited by this method, champion solar modules show a power conversion efficiency of 14.7% on an active area of 12.0 cm^2 and an outstanding shelf

1 stability (only 3.6% relative PCE decay after 3600 h aging). Under continuous operation (1 Sun

2 light illumination, maximum power point condition, dry N_2 atmosphere with <5% relative

3 humidity, no encapsulation) our devices show high light-soaking stability corresponding to an

4 average T_{80} lifetime of 535 h on the small area solar cells and 388 h on the solar module.

5

6 **Introduction**

7 Over the past few years, there have been unprecedented advances in solar cells using metal

8 halide perovskite materials as light absorbers.[1-3] A record power conversion efficiency (PCE)

9 of 23.3% has been certified, already surpassing the well-established commercial photovoltaic

10 technologies e.g., multi-crystalline silicon (22.3%), thin film CIGS (22.6%) and CdTe

11 (22.1%).[4] Substantial efforts have also been made to solve other potential issues that may limit

12 the commercialization of this new technology. Less toxic elements (e.g., Sn^{2+}, Bi^{3+}, Ag^{1+}, Sb^{3+})

13 are being tested to replace Pb^{2+}, and PCE has reached 9%.[5-12] Device stability is significantly

14 improved by optimizing the device structure,[13-17] perovskite composition[18] and deposition

15 technologies[19-21]. Research focus is now shifting to development of reliable perovskite

16 deposition technologies that would allow mass production in industry. To manufacture products

17 with commercially viable module size and yield, the factors that are often ignored in making

18 small-size cells in research labs can have a strong impact on levelized cost of electricity (LCOE)

19 and must be considered.[22-25] These factors include (i) solar cell PCE should be maintained or

20 only decrease slightly upon increasing the active area from the small solar cell scale (active area

21 ~ 0.1 cm^2) towards the solar module scale (> active area ~ 10 cm^2); (ii) Pb waste should be

22 minimized during the deposition process; (iii) the perovskite film deposition methods should

23 be transferable to industry.

24 Considering these factors, the methods developed in research labs may not be all suitable for

25 mass production. For example, most high-performing perovskite solar cells (PCE >20%) are

26 prepared by the anti-solvent based spin-coating method on small active areas (~ 0.1 cm^2).

1   However film uniformity becomes significantly poorer upon increasing the active area to a

2   module scale due to the short precursor-processing window, leading to decreased device

3   performance and reproducibility.[26-28] The inherently high Pb waste (> 90%) during the spin-

4   coating process,[29] the associated cost of waste disposal, and the environmental impact also

5   make this method unsuitable. On the basis of these considerations, a series of scalable

6   perovskite deposition technologies are being developed including blade coating,[26, 30-31] slot die

7   coating,[32] spray coating,[33-41] ink-jet printing,[42] screen printing,[43] chemical vapor deposition,[44-

8   45] pressure-processed coating[46] etc. However, devices based on these technologies typically

9   show much lower PCEs than those achieved in research labs on small size cells. Perovskite

10   films coated using these technologies are formed either by a one-step or a sequential conversion

11   process. Remeika *et al*. reported that the sequential conversion shows clear advantages over

12   one step deposition in the scalable technologies because functional film formation is separated

13   from film coating, allowing separate optimization of the two processes.[29]

14   In this work we develop an upscalable perovskite deposition technology combining raster

15   ultrasonic spray coating and chemical vapor deposition (RUS-CVD). $FAPbI_xBr_{3-x}$ (FA =

16   formamidinium) perovskite films are deposited on FTO/ c-TiO_2 substrates via a sequential

17   deposition method (**Figure 1A**). First, PbI_2 films are prepared by raster ultrasonic spray-coating

18   (RUS) using a precursor solution containing a solvent mixture of DMF and DMSO (Figure 1B

19   and movie S1). PbI_2 films are converted to $FAPbI_xBr_{3-x}$ by CVD in the vapor of formamidinium

20   iodide (FAI), formamidinium bromide (FABr) and methylammonium chloride (MACl) (Figure

21   1C). The RUS-CVD method can address the aforementioned issues.

22   No limitation with respect to the substrate size. The spray coating methods can be divided

23   to three categories based on the operation modes: (a) Stationary spray with the spray head

24   completely fixed; (b) single-pass spray with the spray head only movable in one direction and

25   (c) raster spray with the spray head movable in both x and y directions. Almost all the reported

26   spray coating methods for perovskite deposition use either stationary spray[38, 40] or single-pass

1   spray[33, 34, 36]. Attempting to coat two adjacent areas by stationary or single pass coating would

2   create an overlapped area dense with defects (see Supplementary Information for details of

3   raster coating vs. stationary or single-pass coating). Therefore although spray-coating is a

4   scalable deposition method, most of the reports are on the small cells (active area ≤ 1 cm^2).

5   Uličná et al. reported a scalable perovskite deposition method using the raster spray-coating,[35]

6   but the active area of their devices was only 0.06 cm^2. Hilt et al. reported a rapid spray plasma

7   processing method,[39] but the authors only demonstrated the fabrication of small-area solar cells,

8   not solar modules. By controlling the precursor film drying process, we report a uniform PbI$_2$

9   film deposition method based on a raster ultrasonic spray process on substrates with a size of

10   10 cm x 10 cm, which to our best knowledge, is the first report in the perovskite research

11   community to demonstrate continuously scalable spray coating with a pattern width not limited

12   by the size of the spray head. The subsequent conversion from PbI$_2$ to perovskite via CVD has

13   also been shown to be scalable[47-49] and with weak substrate size dependence[44]. The reaction

14   speed during the CVD step is slower than other open air processing methods, such as blade

15   coating. However, considering that a large number of large area substrates can be processed

16   simultaneously in a large CVD setup[45], the deposition time per substrate is expected to be

17   substantially shorter.

18   Solar cell performance shows much lower substrate-size dependence than the mostly used

19   spin-coating method, owing to the high film uniformity and quality at large scale. (Figure 1D)

20   Low lead waste. PbI$_2$ precursor utilization efficiency increases to almost 100% upon

21   increasing substrate size (78% for 1.5 cm x 1.5 cm, 92% for 5 cm x 5 cm, 96% for 10 cm x 10

22   cm, 99% for 30 cm x 30 cm, see the experimental section), significantly higher than the mostly

23   used spin-coating method (less than 10% Pb utilization at different substrate sizes). (Figure 1E)

24   Transferable to industry. Ultrasonic spray coating is widely used in industry for display and

25   lens coating, active layer and anti-reflection coating for solar cells, etc.[50] CVD is also a mature

26   coating technology widely utilized in the thin film solar cell industry.[47-49]

1   It is important to note that widely employed single point local characterization methods that are

2   suitable for small solar cells (e.g., active area ~ 0.1 cm^2) are no longer sufficient for

3   characterizing mini-modules (> 10 cm^2 active area).[39] To study thin film properties across large

4   area, UV-Vis spectroscopy, X-ray diffraction (XRD), atomic force microscopy (AFM), cross-

5   section scanning electron microscopy (SEM) and photoluminescence mapping are used to

6   characterize multiple locations on the 5 cm x 5 cm photoactive layers, to ensure the absorbance,

7   crystallinity and surface roughness are representative of the large area device. In addition, we

8   study film properties using large-area compatible characterization methods such as scattered

9   light intensity (SLI) imaging and electroluminescence (EL) imaging, which allow rapid

10 characterization of the entire 5 cm x 5 cm mini-modules and are also compatible with in-line

11 characterization in a production environment. With $FAPb(I_{0.85}Br_{0.15})_3$ perovskite layer

12 deposited by our method, perovskite mini-modules using the standard device architecture (i.e.,

13 with a TiO_2 electron transporting layer, a spiro-MeOTAD hole transporting layer, and a gold

14 electrode) show a champion module performance of 14.7% on an active area of 12.0 cm^2. Under

15 continuous operation (constant 1 Sun light illumination, maximum power point, MPP, N_2

16 atmosphere, <5% relative humidity, no encapsulation) devices show high stability

17 corresponding to an average T_{80} lifetime of 535 h on the small cells (based on the statistical

18 data of 4 small cells) and 388 h on the module.

19 **Results and discussion**

20 **PbI_2 deposition by RUS.**

21 Several groups have reported using a co-solvent of DMF and DMSO mixture for the perovskite

22 precursor in the spin-coating process and the ratios are between 10:1 to 4:1 (V:V) to achieve

23 uniform perovskite deposition.[18, 51] However, our initial results based on single-pass ultrasonic

24 spray (SUS)-coated PbI_2 suggest that this optimized ratio for perovskite is not directly

25 applicable to spray-coating PbI_2 due to the different crystallization dynamics.[34] Generally, a

26 higher DMSO concentration leads to a longer evaporation time because of its higher boiling

1   point and higher solubility for PbI_2 stemming from its higher coordination number, but a lower

2   viscosity. [52-54] Uniformity of the PbI_2 layer changes substantially as we vary the ratio between

3   DMF and DMSO in the RUS process. The optimal PbI_2 deposition by SUS is not suitable for

4   the RUS process. Therefore we optimize the DMF:DMSO ratio for PbI_2 deposition via RUS

5   starting from 14:1 (volume ratio) according to our reported SUS method.[34] Four types of solvent

6   mixtures with the DMF:DMSO ratio varying from 14:0.5 to 14:1 are employed to dissolve PbI_2.

7   SLI mapping measurements are performed on the entire 5 cm × 5 cm sprayed PbI_2 precursor

8   and annealed films. Different SLI is either caused by different surface roughness or different

9   amount of micro cracks in the film bulk (see Supplemental Information for details on the SLI

10 mapping measurement). We observe that low DMSO concentration in the co-solvent, i.e.,

11 (DMF : DMSO = 14 : 0.5) results in a PbI_2 precursor film with high SLI that resembles the film

12 coated using pure DMF solvent (**Figure 2A**).[32] The high SLI remains after the film is annealed

13 (Figure 2E). Medium DMSO concentration (DMF : DMSO = 14 : 0.65) results in translucent

14 PbI_2 precursor films with low SLI (Figure 2B), which remains after annealing (Figure 2F). High

15 DMSO concentrations (DMF : DMSO = 14 : 0.85 and DMF : DMSO = 14 : 1) result in slightly

16 increased SLI again for the PbI_2 precursor films (Figure 2C and 2D). The SLI increased strongly

17 after annealing (Figure 2G and 2H), due to formation of the internal cracks and voids caused

18 by evaporation of DMSO. [55] AFM measurements are carried out on 6 different locations of each

19 5 cm × 5 cm PbI_2 film to study the surface roughness. RMS roughness decreases drastically

20 with DMSO concentration increasing from low (DMF : DMSO = 14 : 0.5) to medium (DMF :

21 DMSO = 14 : 0.65) and decreases slightly with further increasing the DMSO concentration

22 (DMF : DMSO = 14 : 0.85 and DMF : DMSO = 14 : 1) (Figure 2I and **Figure S1**). We interpret

23 the SLI and AFM data as follows. A low DMSO concentration (DMF : DMSO = 14 : 0.5) in

24 the solvent mixture results in a dense PbI_2 film with rough surface. While high DMSO

25 concentrations (DMF : DMSO = 14 : 0.85 and DMF : DMSO = 14 : 1) result in a smooth film

26 surface but with a large amount of internal cracks and voids (Figure 2J-M). A medium DMSO

1 concentration results in a smooth PbI_2 film with negligible internal cracks and voids. A rough

2 PbI_2 film will convert to a rough perovskite film, which is detrimental for the solar cell

3 performance.[34] Therefore low DMSO concentration (DMF : DMSO = 14 : 0.5) is not preferred.

4 To compare performance between the perovskite films formed from compact PbI_2 and the films

5 containing internal cracks and voids, we select two DMSO ratios (DMF :DMSO = 14 :0.65 and

6 DMF :DMSO = 14 :1) for the perovskite conversion.

7 **$FAPb(I_xBr_{1-x})_3$ formation by RUS-D and RUS-CVD.**

8 The two type of RUS-coated PbI_2 films are then reacted with FAI, FABr and MACl to form

9 $FAPb(I_xBr_{1-x})_3$ perovskite via two approaches, i.e., a CVD (designated as RUS-CVD) and an

10 optimized dipping approach reported by our group (designated as RUS-D).[34] Perovskite films

11 converted from the compact PbI_2 (DMF : DMSO = 14 : 0.65 for RUS) show high uniformity

12 with low SLI over the entire 5×5 cm substrate area (**Figure 3A and 3B**) and low surface

13 roughness (RMS roughness 25.2±0.5 nm for RUS-CVD and 33±5 nm for RUS-D) (Figure 3E,

14 3F, 3I, 3J, 3K; see Supplementary Information for statistical AFM results, **Figure S2**). We also

15 performed cross-section SEM measurements on multiple sample locations. All the SEM images

16 consistently show that the films converted from the compact PbI_2 (DMF : DMSO = 14 : 0.65

17 for RUS) have a high degree of uniformity (**Figure S3** and **Figure S4**). On the other hand, films

18 converted from the PbI_2 layers with internal cracks (DMF : DMSO = 14 : 1 for RUS) show poor

19 macroscopic uniformity with lots of spots (Figure 3C and 3D), and high surface roughness with

20 many microscopic pin-holes (RMS roughness 75±6 nm for RUS-CVD and 55±6 nm for RUS-

21 D) (Figure 3G, H, L, M and Figure S3). In addition, CVD converted perovskite shows larger

22 grain size than dipping converted perovskite (Figure 3E, 3F and Figure S4). Because pinholes

23 in the perovskite films are detrimental to the device performance[56], we select the compact PbI_2

24 films deposition process (DMF : DMSO = 14 : 0.65) to study the effect of conversion process

25 on the film composition and optical property.

1   FAPb$(I_xBr_{1-x})_3$ with x equal to 85% is employed as the target perovskite material owing to its

2   superior thermal stability as reported by previous studies.[57-59] For the films prepared by the

3   RUS-D method, the Br^- to (I^- + Br^-) molar ratio is around 15% according to their ratio in the

4   dipping solution. To make the two conversion methods comparable, we optimize the RUS-CVD

5   process so as to prepare the perovskite with the similar composition. XRD and UV-Vis

6   measurements are performed on 6 different locations of each 5 cm × 5 cm substrate to study the

7   composition of the perovskite films (**Figure 4A**). Perovskite films converted by RUS-CVD and

8   RUS-D show very similar XRD peak positions at 14.1°, 24.5°, 28.3°, 31.8°, 33.7°, assigned to

9   (-111), (021), (222), (231), (030) perovskite crystal planes, respectively, suggesting that the

10   perovskite films are of a similar composition (Figure 4B). Peak positions agree well with those

11   of FAPb$(I_{0.85}Br_{0.15})_3$.[58] The peaks at 26.4°, 37.7° belong to the FTO substrate. RUS-CVD

12   processed perovskite film shows much higher intensity of the (-111), (222) and (231) diffraction

13   peaks but lower XRD intensity at (021) than the RUS-D processed perovskite film. These

14   results suggest that the perovskite films prepared by different methods show different

15   crystalline alignment and RUS-CVD processed perovskite film shows a higher overall degree

16   of crystallinity. Moreover, perovskite films prepared by RUS-D show clear PbI_2 peaks (12.7°,

17   38.6°), similar to our previous study.[34] XRD patterns on the same sample but different positions

18   are similar, suggesting the data are representative for large area (Figure 4C). To quantify the

19   PbI_2 crystalline phase fraction in the films, we perform the Rietveld refinement based on the

20   XRD results. A negligible PbI_2 phase fraction is determined for the films prepared by RUS-

21   CVD, while 10±1% (wt) PbI_2 is determined for the films prepared by RUS-D (**Table S1**).

22   Although a small amount of PbI_2 existing at the perovskite grain boundary is reported to be

23   beneficial for the defect passivation,[60] such a large amount of PbI_2 is expected to be detrimental

24   to the solar cell performance, due to the absorbance loss. To verify this point, we conduct UV-

25   Vis spectroscopy measurements on these films. Indeed, absorbance is lower for the films

26   prepared by RUS-D (Figure 4D). Furthermore, variation of the absorbance at same sample but

8

1 different positions is 6-8 times smaller for the RUS-CVD method at wavelength between 600

2 – 700 nm, suggesting the RUS-CVD prepared perovskite film is more uniform at the

3 macroscopic scale (detection area is 0.3 cm × 0.5 cm for each measurement) (Figure 4D inset).

4 Absorbance edges for the two perovskite films are both at ~790 nm, agreeing well with that for

5 the $FAPb(I_{0.85}Br_{0.15})_3$ perovskite.[58]

6 **Effect of MACl during the perovskite formation.**

7 MACl is added for both dipping and CVD conversion processes. In the dipping process, MACl

8 strongly affects the perovskite crystallization process and leaves the films after thermal

9 annealing.[61] We find that creation of MACl atmosphere during the perovskite formation via the

10 CVD process also influences the perovskite crystallization, resulting in increase of the

11 perovskite (-111) and (222) peak intensity (**Figure S5A and S5B**) and reduced perovskite film

12 surface roughness (Figure S5C and S5D). Perovskite converted via CVD with or without MACl

13 atmosphere shows negligible change in the XRD peak position, suggesting that the Cl^- amount

14 incorporated into the perovskite lattice is not significant (Figure S5B).[62] To study whether FA^+

15 is partially substituted by the MA^+ cation, we conduct high resolution X-ray photoelectron

16 spectroscopy (HRXPS) measurements on the two $FAPb(I_{0.85}Br_{0.15})_3$ perovskite prepared by

17 RUS-CVD and RUS-D and also on the RUS-CVD prepared $MAPbI_3$ and $FAPbI_3$ perovskite as

18 control. Little peak position change appears for the Pb 4f and I 3d regions comparing the four

19 samples (**Figure S6A and S6B**). Br 3d signals appear in the two $FAPb(I_{0.85}Br_{0.15})_3$ perovskite

20 films (Figure 4E). Two peaks at 288.5 and 284.8 eV assigned to FA^+ related C 1s peaks appear

21 for the two $FAPb(I_{0.85}Br_{0.15})_3$ perovskite films and no typical MA^+ peak (286.5 eV) appears,

22 indicating that no or only a very small amount of MA^+ substitutes the FA^+ position (Figure

23 4F).[19, 44] The statement is further confirmed by the N 1s peak position. The two

24 $FAPb(I_{0.85}Br_{0.15})_3$ perovskite films show the N 1s peak at 400.7 eV similar to $FAPbI_3$, where

25 the N 1s peak associated with MA^+ appears at 402.5 eV (Figure 4G).[19, 44] PL mapping is a

26 spatially resolved technique that can characterize uniformity and quality of the photoactive

1 layer. We carry out the PL mapping measurements on 4 different positions of each perovskite

2 film (detection area is 80 μm × 80 μm) and quantitatively compare the PL emission results. The

3 CVD-converted perovskite films show not only a ~10% higher PL intensity, but also ~5 times

4 narrower PL intensity distribution than dipping-converted perovskite (Figure 4H, 4I, 4J, **Figure**

5 **S7A-H**). Based on the results, we conclude that perovskite films prepared by RUS-CVD

6 method reveal higher uniformity across large area and higher quality than RUS-D from the

7 purity, crystallinity and optical property point of view.

8 **Perovskite solar cell/module performance and reproducibility.**

9 To study the device performance, we prepare perovskite modules by RUS-CVD and RUS-D on

10 5 cm × 5 cm substrates, where each contains 6 cells connected in series with a total active area

11 of 12.0 cm^2 (**Figure 5A**). A patterned TiO_2 layer was deposited by a scalable vacuum sputtering

12 method as the elerctron transporting layer.[63-64] No mesoporous TiO_2 layer is used because of

13 the patterning difficulty. We are not aiming at demonstrating deposition methods for the

14 complete perovskite solar module. Therefore the deposition process for other layers (e.g., hole

15 transport layer) may not be scalable. The modules are patterned by 3 shadow masks. Details of

16 the module geometry are shown in **Figure S8** and discussed in the supporting information.[44] J-

17 V measurements are conducted on the modules with 1 to 6 cells connected in series to determine

18 the performance on different device active area. The champion module prepared by the RUS-

19 CVD shows a V_{oc} of 6.29 V, I_{sc} of 42.6 mA, FF of 66.5%, and PCE of 14.7% for the 6 sub-cells

20 connected in series from forward to backward scan (Figure 5B) and a PCE of 13.5% from

21 backward to forward scan (**Figure S9A**). As far as we know, this is among the highest

22 performing perovskite solar module prepared by spray-coating method to date.[34, 42, 65] In

23 addition, performance of the champion RUS-CVD modules slowly decreases from 16.1% on 2

24 cm^2 to 14.7% on 12 cm^2 (Figure 5D and **Table S2**), corresponding to a very low PCE loss/area

25 (defined as ($PCE_{single cell}$ − PCE_{module})/($area_{module}$ − $area_{single cell}$)) of 0.14 %/cm^2.[44] On the other

26 hand, the champion module prepared by RUS-D shows a much lower PCE of 8.6% from

1   forward to backward scan and a PCE of 6.8% from backward to forward scan (Figure 5C and

2   Figure S9B). Performance of the champion RUS-D modules decreases much faster from 13.3%

3   on 2 cm^2 to 8.6% on 12 cm^2 (Figure 5D and Table S2), corresponding to a high PCE loss/area

4   (defined as ($PCE_{single\ cell}$ − PCE_{module})/($area_{module}$ − $area_{single\ cell}$)) of 0.47 %/cm^2. Such a big PCE

5   loss/area gap between the two perovskite processing methods indicates that the RUS-CVD

6   perovskite shows higher uniformity and lower series resistance at the perovskite absorber and

7   related interfaces (see Supplementary Information for details of the reasons causing the module

8   performance decrease upon increase of the active area).

9   To study the reproducibility of the two perovskite fabrication approaches, 16 modules (8

10   modules prepared by RUS-CVD and 8 modules prepared by RUS-D) are prepared for statistical

11   analysis. Averaged PCEs are 14.2±0.3% (12 cm^2 active area) for RUS-CVD prepared modules,

12   significantly higher than RUS-D prepared modules (6±1%) (Figure 5E). It is worth mentioning

13   that even for the modules prepared by RUS- D, the PCE has already exceeded that for the solar

14   module based on the perovskite film prepared by the combination of SUS-coated PbI_2 and

15   dipping conversion (~8% champion module PCE on 10 cm^2 active area).[34] This result indicates

16   the advantage of the RUS process over our previously reported SUS process in PbI_2 deposition

17   across large area. With perovskite film converted by CVD, the module performance is further

18   increased by 136.6% (PCE increase = (average $PCE_{RUS-CVD}$- average PCE_{RUS-D}) /average

19   PCE_{RUS-D}) than those converted by our reported dipping process. RUS-CVD prepared modules

20   shows only marginally higher average J_{sc} than RUS-D prepared modules, suggesting that J_{sc} is

21   not the main factor causing the performance variation. This is confirmed by external quantum

22   efficiency (EQE) measurements. The integrated currents are both 20.3 mA/cm^2 for champion

23   modules prepared by RUS-D and RUS-CVD, agreeing well with the current values from J–V

24   measurement with variations of less than 5% (Figure S9C). Module performance differences

25   are mainly caused by differences in V_{oc} and FF according to the statistical results (Figure 5F-

26   H), which can be related to the different perovskite film quality and uniformity.[44]

Perovskite solar module quality and uniformity.

To evaluate device quality and uniformity over the entire module area we performed spatially resolved electroluminescence (EL) measurements.[66] While PCE depends linearly on V_{oc}, I_{sc}, and FF, EL intensity (LED efficiency) at a given current is exponentially dependent on quasi-Fermi level separation (V_{oc}).[67] Exponential dependence on V_{oc} leads to a much weaker dependence on FF, and EL intensity probes the quality (non-radiative recombination rate) in the absorber without sensitivity to resistive losses that would reduce measured FF in a PCE measurement. Comparison of EL measurements between RUS-CVD and RUS-D modules shows that RUS-D modules have a lower EL intensity in most locations whereas RUS-CVD modules have dramatically higher EL intensity at the same applied current (Figure 5I and 5J). We plot the EL intensity histogram figure to evaluate the EL intensity as a function of frequency. RUS-D module shows a wide EL intensity distribution between 0-30% relative to the saturated EL intensity, while RUS-CVD module shows over 90% distribution at the saturated EL intensity (Figure 5K and 5K inset). Such dramatic differences in EL intensity suggest that the RUS-CVD prepared perovskite has much less non-radiative recombination centers induced by defects, which contributes to a higher module V_{oc} and PCE.

Perovskite solar cell/module operational stability.

Instability is one of the main challenges for perovskite solar cells. Because perovskite solar cell lifetime varies substantially for different perovskite deposition methods, it is necessary to report the device lifetime for newly developed methods. Conditions for the device stability test such as atmosphere, temperature, illumination (continuous light soaking or storage under dark) and load applied (open circuit, short circuit or MPP) significantly affect the device lifetime.[68] Device stability evaluation based on statistical results is also recommended.[69] Considering these reasons, we prepare 8 $FAPb(I_{0.85}Br_{0.15})_3$ perovskite solar cells (0.1 cm^2 active area) in two different batches (4 cells prepared by RUS-CVD and 4 cells prepared by RUS-D) and conduct the first operational stability measurements on these devices. The devices are kept at continuous

12

1 sun illumination near their MPP, in the N_2 atmosphere (<5% relative humidity), without

encapsulation at room temperature (25.0 ˚C) and measured by step J-V scans every 30 min

(**Figure S10A and S10B**). Similar to other reports, RUS-CVD prepared devices show the initial

transient PCE decay (i.e., the exponential regime), which is followed by the linearly decay (i.e.,

the linear regime) (**Figure 6A**).[68] Transient decay is generally recoverable if the device is stored

in dark for an extended time.[68] Therefore the T_{80} parameter, which represents the time when

PCE decays to 80%, can be calculated based on the linear decay regime.[68] RUS-CVD prepared

devices show an average T_{80} value of 535 h (Figure 6A brown line to green line), closing to the

highest reported lifetime for planar structured perovskite solar cells.[13] Such a high T_{80} lifetime

suggests that RSU-CVD prepared devices are very stable under the operational condition. In a

previous study, we report the poor device stability for the CVD converted $FAPbI_3$ perovskite

solar modules due to formation of the yellow non-perovskite phase.[44] Here we demonstrate that

by adding 15% Br in the perovskite, stability of the perovskite solar cells is significantly

improved. We find all of the J_{sc}, V_{oc} and FF decay with time and the majority of PCE decay

comes from the FF (Figure 6B-D). In comparison, RUS-D prepared devices decay linearly at a

much higher rate, corresponding to an average T_{80} value of 8 h (Figure 6A). Different from

RUS-CVD prepared device, J*sc* of RUS-D prepared devices increase by 20% until reaching the

maximum value and then decrease constantly (Figure 6C inset). The majority factor casing the

PCE decay is J_{sc}, not the FF (Figure 6B-D). The nearly 70 times larger T_{80} value for the RUS-

CVD prepared device than the RUS-D case suggests the excellent long-term stability of the

cells based on our RUS-CVD method.

So far, most of the operational stability tests are conducted on small-sized solar cells (e.g.,

active area ~ 0.1 cm^2), not large-sized perovskite solar modules. The non-uniformity issue of

the perovskite film is more pronounced on the enlarged substrate, which has more changes to

cause the device failure under operation. On the other hand, temperature of the module increases

greatly under continuous illumination, which may also affect their performance and lifetime.[45]

1 Thus, it is important to study the operational stability of the perovskite modules at elevated

2 temperature. Here, we conduct the operation stability measurements at the similar condition as

3 for small cells on the $FAPb(I_{0.85}Br_{0.15})_3$ perovskite solar modules (active area 12 cm^2). We

4 monitor the temperature during the operational stability measurements and find that the

5 temperature rapidly increases from 25.0 ˚C to > 46.0 ˚C during the first 1000 s (Figure 6E) and

6 stabilizes in the following period (Figure 6F). RUS-CVD prepared module follows the PCE

7 decay behavior of RUS-CVD prepared small cells, including an initial exponential decay

8 regime and a linear decay regime (Figure 6E and 6F). After 1200 min operation, the module

9 still shows a PCE of 13.3%, with only 0.2% PCE decay comparing to the module PCE after an

10 initial transient decay. This result suggests that the RUS-CVD prepared device is quite stable

11 at temperature of up to 46.0 ˚C. We measured the operation stability of another RUS-CVD

12 prepared perovskite module under the same condition until the device decayed to less than 80%

13 of its initial PCE. The RUS-CVD prepared device shows a long T_{80} lifetime of 388 h (Figure

14 6G brown line to green line). Comparing with the very few operational stability reports on the

15 perovskite solar modules[46, 70], our RUS-CVD prepared module is very stable under such

16 measurement conditions. In comparison, RUS-D prepared perovskite module shows 65% PCE

17 decay from 8.1% to 2.8% after 1200 min operation. In addition, we also study the module

18 storage stability. One RUS-CVD prepared module and one RUS-D prepared module are stored

19 in dark N_2 atmosphere (15% relative humidity) and measured in ambient air (~50% relative

20 humidity). After 3600 h, RUS-CVD prepared module still shows a PCE of 13.4%, with a

21 relative PCE decay of 3.6% (Figure 6H). In comparison, RUS-D prepared module shows a PCE

22 of 3.3% and a relative PCE decay of 47.4%. Based on all the stability results, we think the RUS-

23 CVD method is not only a scalable perovskite deposition method but also present promising

24 device stability on the solar module size.

25 **Perovskite decomposition and ion migration under operation condition**

1 Furthermore, we study the reason causing the different device operational stability. Perovskite

2 solar cells fail under operation or storage for several reasons, such as light-, thermal- oxygen-

3 and humidity-induced perovskite degradation[71-75], charge transporting layer decomposition[76-77],

4 ion migration[78-79] etc. Because the only difference in the two conditions comes from the

5 perovskite film, the perovskite degradation and ion migration can be considered as the main

6 factors that affect the device stability. We prepare perovskite solar cells by the two methods

7 and perform XRD and UV-vis measurements on these samples. Each method includes a fresh

8 device, the same device after 40 h storage in dark and N_2 atmosphere and one operated device

9 under MPP condition for 40 h. Gold electrodes are removed before measurements. Devices

10 prepared by RUS-CVD show negligible change in XRD pattern after storage in dark N_2

11 atmosphere or operation (**Figure 7A**). On the other hand, the XRD peaks assigned to the

12 perovskite significantly decreased after 40 h operation for the RUS-D prepared devices (Figure

13 7B). The RUS-D prepared perovskite stored in dark N_2 atmosphere does not decompose,

14 indicating that decomposition of perovskite is caused by the operation (light, bias). The

15 statement is further confirmed by the UV-vis absorbance spectroscopy results. There is little

16 change in the absorbance for the devices prepared by RUS-CVD (Figure 7C), but there has been

17 an obvious reduction in the absorbance between the wavelength of 500 and 790 nm, which can

18 be assigned to decomposition of perovskite material, for the operated device prepared by RUS-

19 D (Figure 7D). Instability of the perovskite material in turn affects the operation instability of

20 the device. Such a different perovskite material stability might be caused by the different

21 perovskite grain size (Figure 3E and 3F).[80] To better understand the composition changes and

22 ion migration that relate to the device failure, we perform the second ion mass spectrometry

23 (SIMS) measurements on fresh and operated devices (40 h under MPP condition) prepared by

24 RUS-CVD and RUS-D. Operated devices are stored in the dark N_2 atmosphere for 1-3 days

25 before the SIMS measurements, so the changes observed are irreversible ones.[81] Signals of Au^+,

26 Pb^+, FA^+, I^+, Br^+, Ti^+, Sn^+ appear sequentially in all of the 4 samples (**Figure S11**). We observe

no significant difference of the element distribution (FA^+, Au^+, Pb^+, I^+, Br^+, Ti^+, Sn^+) between fresh and operated devices that are prepared by RUS-CVD (Figure 7E and Figure S11). However, we identify a redistribution and an intensity decrease of FA^+ on RUS-D prepared device after operation (Figure 7F). It has been reported that the FA^+ redistribution can cause the failure of the device after operation.[81] Similar to the report, we do not see obvious I^+ and Br^+ migration.[81] The FA^+ migration is likely to be another key factor causing the failure of the RUS-D prepared device after operation at such a time scale. Taken together, the high operational stability of RUS-CVD prepared devices could be explained by the robust perovskite film with negligible decomposition and FA^+ ion migration at such a time scale. These results confirm the excellent stability of perovskite solar cells and modules based on our RUS-CVD method. Comparing with the perovskite films processed by solution based methods when the perovskite is usually formed by annealing for 20 min, the growth rate of CVD-processed perovskite is much slower. The constant supply of organic halide vapors helps the perovskite recrystallize through in situ annealing, leading to formation of high quality perovskite films.[55]

Conclusions

In summary, we develop a scalable perovskite deposition technology with combination of raster ultrasonic spray coating and chemical vapor deposition. Our technology overcomes the coating size limitation of the existing stationary spray and single-pass spray. Negligible lead waste during the PbI_2 deposition process makes this technology environmental friendly and transferable to industry. $FAPb(I_{0.85}Br_{0.15})_3$ perovskite films prepared using this technology show high quality and uniformity. Planar structured perovskite module fabricated basing on this method shows a high module PCE of 14.7% on an active area of 12.0 cm^2, closing to the highest reported module performance with perovskite film deposited by ultrasonic spray-coating. The device also shows high operational stability, corresponding to an average T_{80} lifetime of 535 h on the small cells (0.1 cm^2) and 388 h on the module (12 cm^2).

1 **Supporting Information**
2 Supporting Information is available from the Wiley Online Library or from the author.
3

10 **Conflict of interest**

11 The authors declare no conflict of interest.
12

13 References

14 [1]   J. Burschka, N. Pellet, S. J. Moon, R. Humphry-Baker, P. Gao, M. K. Nazeeruddin, M.

15 Grätzel, *Nature* **2013**, *499*, 316-319.

16 [2]   H. S. Kim, C. R. Lee, J. H. Im, K. B. Lee, T. Moehl, A. Marchioro, S. J. Moon, R.

17 Humphry-Baker, J. H. Yum, J. E. Moser, M. Grätzel, N. G. Park, *Sci. Rep.* **2012**, *2*, 591.

18 [3]   M. Liu, M. B. Johnston, H. J. Snaith, *Nature* **2013**, *501*, 395-398.

19 [4]   National   Renewable   Energy   Laboratory   (NREL).

20 http://www.nrel.gov/ncpv/images/efficiency_chart.jpg (accessed Febrary, 2018).

21 [5]   W. Ke, C. C. Stoumpos, M. Zhu, L. Mao, I. Spanopoulos, J. Liu, O. Y. Kontsevoi, M.

22 Chen, D. Sarma, Y. Zhang, M. R. Wasielewski, M. G. Kanatzidis, *Sci. Adv.* **2017**, *3*, e1701293.

23 [6]   F. Jiang, D. Yang, Y. Jiang, T. Liu, X. Zhao, Y. Ming, B. Luo, F. Qin, J. Fan, H. Han,

24 L. Zhang, Y. Zhou, *J Am. Chem. Soc.* **2018**, *140*, 1019-1027.

25 [7]   W. Ke, C. C. Stoumpos, I. Spanopoulos, L. Mao, M. Chen, M. R. Wasielewski, M. G.

26 Kanatzidis, *J. Am. Chem. Soc.* **2017**, *139*, 14800-14806.

27 [8]   Y. Liao, H. Liu, W. Zhou, D. Yang, Y. Shang, Z. Shi, B. Li, X. Jiang, L. Zhang, L. N.

28 Quan, R. Quintero-Bermudez, B. R. Sutherland, Q. Mi, E. H. Sargent, Z. Ning, *J. Am. Chem.*

29 *Soc.* **2017**, *139*, 6693-6699.

[9]   R. Nie, A. Mehta, B. W. Park, H. W. Kwon, J. Im, S. I. Seok, *J. Am. Chem. Soc.* **2018**, *140*, 872-875.

[10]   S. Shao, J. Liu, G. Portale, H.-H. Fang, G. R. Blake, G. H. ten Brink, L. J. A. Koster, M. A. Loi, *Adv. Energy Mater.* **2018**, *8*, 1702019.

[11]   A. H. Slavney, T. Hu, A. M. Lindenberg, H. I. Karunadasa, *J. Am. Chem. Soc.* **2016**, *138*, 2138-2141.

[12]   X. G. Zhao, J. H. Yang, Y. Fu, D. Yang, Q. Xu, L. Yu, S. H. Wei, L. Zhang, *J. Am. Chem. Soc.* **2017**, *139*, 2630-2638.

[13]   H. Tan, A. Jain, O. Voznyy, X. Lan, F. P. G. D. Arquer, J. Z. Fan, R. Quintero-Bermudez, M. Yuan, B. Zhang, Y. Zhao, F. Fan, P. Li, L. N. Quan, Y. Zhao, Z.-H. Lu, Z. Yang, S. Hoogland, E. H. Sargent, *Science* **2017**, *355*, 722-726.

[14]   S. S. Shin, E. J. Yeom, W. S. Yang, S. Hur, M. G. Kim, J. Im, J. Seo, J. H. Noh, S. I. Seok, *Science* **2017**, *356*, 167-171.

[15]   K. A. Bush, A. F. Palmstrom, Z. J. Yu, M. Boccard, R. Cheacharoen, J. P. Mailoa, D. P. McMeekin, R. L. Z. Hoye, C. D. Bailie, T. Leijtens, I. M. Peters, M. C. Minichetti, N. Rolston, R. Prasanna, S. Sofia, D. Harwood, W. Ma, F. Moghadam, H. J. Snaith, T. Buonassisi, Z. C. Holman, S. F. Bent, M. D. McGehee, *Nat. Energy* **2017**, *2*, 17009.

[16]   L. Qiu, L. K. Ono, Y. Jiang, M. R. Leyden, S. R. Raga, S. Wang, Y. B. Qi, *J. Phys. Chem. B* **2018**, *122*, 511-520.

[17]   F. Bella, G. Griffini, J.-P. Correa-Baena, G. Saracco, M. Grätzel, A. Hagfeldt, S. Turri, C. Gerbaldi, *Science* **2016**, *354*, 203-206.

[18]   M. Saliba, T. Matsui, K. Domanski, J.-Y. Seo, A. Ummadisingu, S. M. Zakeeruddin, J.-P. Correa-Baena, W. R. Tress, A. Abate, A. Hagfeldt, M. Grätzel, *Science* **2016**, *354*, 206-209.

[19]   Y. Jiang, E. J. Juarez-Perez, Q. Ge, S. Wang, M. R. Leyden, L. K. Ono, S. R. Raga, J. Hu, Y. B. Qi, *Mater. Horiz.* **2016**, *3*, 548-555.

1 [20] W. Chen, Y. Wu, Y. Yue, J. iu, W. Zhang, X. Yang, H. Chen, E. Bi, I. Ashraful, M.

2 Grätzel, L. Han, *Science* **2015**, *350*, 944-948.

3 [21] S. R. Raga, Y. Jiang, L. K. Ono, Y. B. Qi, *Energy Technol.* **2017**, *5*, 1750-1761.

4 [22] M. Cai, Y. Wu, H. Chen, X. Yang, Y. Qiang, L. Han, *Adv. Sci.* **2017**, *4*, 1600269.

5 [23] Z. Song, C. L. McElvany, A. B. Phillips, I. Celik, P. W. Krantz, S. C. Watthage, G. K.

6 Liyanage, D. Apul, M. J. Heben, *Energy Environ. Sci.* **2017**, *10*, 1297-1305.

7 [24] N. L. Chang, A. W. Y. Ho-Baillie, P. A. Basore, T. L. Young, P. Evans, *Prog. Photovolt:*

8 *Res. Appl.* **2017**, *25*, 390-405.

9 [25] N. L. Chang, A. W. Y. Ho-Baillie, D. Vak, M. Gao, M. A. Green, R. J. Egan, *Sol. Energy*

10 *Mater. Sol. Cells* **2018**, *174*, 314-324.

11 [26] M. Yang, Z. Li, M. O. Reese, O. G. Reid, D. H. Kim, S. Siol, T. R. Klein, Y. Yan, J. J.

12 Berry, M. F. A. M. van Hest, K. Zhu, *Nat. Energy* **2017**, *2*, 17038.

13 [27] Z. Li, T. R. Klein, D. H. Kim, M. Yang, J. J. Berry, M. F. A. M. van Hest, K. Zhu, *Nat.*

14 *Rev. Mater.* **2018**, *3*, 18017.

15 [28] J. J. Berry, J. van de Lagemaat, M. M. Al-Jassim, S. Kurtz, Y. Yan, K. Zhu, *ACS Energy*

16 *Lett.* **2017**, *2*, 2540-2544.

17 [29] M. Remeika, Y. B. Qi, *J. Energy Chem.* **2017**, *27*, 1101-1110.

18 [30] Y. Deng, Q. Wang, Y. Yuan, J. Huang, *Mater. Horiz.* **2015**, *2*, 578-583.

19 [31] M. Yang, D. H. Kim, T. R. Klein, Z. Li, M. O. Reese, B. J. Tremolet de Villers, J. J.

20 Berry, M. F. A. M. van Hest, K. Zhu, *ACS Energy Lett*., **2018**, *3*, 322-328.

21 [32] G. Cotella, J. Baker, D. Worsley, F. De Rossi, C. Pleydell-Pearce, M. Carnie, T. Watson,

22 *Sol. Energy Mater. Sol. Cells* **2017**, *159*, 362-369.

23 [33] S. Das, B. Yang, G. Gu, P. C. Joshi, I. N. Ivanov, C. M. Rouleau, T. Aytug, D. B.

24 Geohegan, K. Xiao, *ACS Photonics* **2015**, *2*, 680-686.

25 [34] M. Remeika, S. R. Raga, S. Zhang, Y. B. Qi, *J. Mater. Chem. A* **2017**, *5*, 5709-5718.

1   [35]   S. Uličná, B. Dou, D. H. Kim, K. Zhu, J. M. Walls, J. W. Bowers, M. F. A. M. van Hest,

2   *ACS Appl. Energy Mater.* **2018**, *1*, 1853-1857.

3   [36]   A. T. Barrows, A. J. Pearson, C. K. Kwak, A. D. F. Dunbar, A. R. Buckley, D. G. Lidzey,

4   *Energy Environ. Sci.* **2014**, 7, 2944-2950.

5   [37]   J. G. Tait, S. Manghooli, W. Qiu, L. Rakocevic, L. Kootstra, M. Jaysankar, C. A. Masse

6   de la Huerta, U. W. Paetzold, R. Gehlhaar, D. Cheyns, P. Heremans, J. Poortmans, *J. Mater.*

7   *Chem. A* **2016**, *4*, 3792-3797.

8   [38]   H. Huang, J. Shi, L. Zhu, D. Li, Y. Luo, Q. Meng, *Nano Energy* **2016**, *27*, 352-358.

9   [39]   F. Hilt, M. Q. Hovish, N. Rolston, K. Brüning, C. J. Tassone, R. H. Dauskardt, *Energy*

10   *Environ. Sci.* **2018**, *11*, 2102-2113.

11   [40]   J. H. Heo, M. H. Lee, M. H. Jang, S. H. Im, *J. Mater. Chem. A* **2016**, *4*, 17636-17642.

12   [41]   J. E. Bishop, J. A. Smith, C. Greenland, V. Kumar, N. Vaenas, O. S. Game, T. J.

13   Routledge, M. Wong-Stringer, C. Rodenburg, D. G. Lidzey, *ACS Appl. Mater. Interfaces* **2018**,

14   *10*, 39428-39434.

15   [42]   S.-G. Li, K.-J. Jiang, M.-J. Su, X.-P. Cui, J.-H. Huang, Q.-Q. Zhang, X.-Q. Zhou, L.-M.

16   Yang, Y.-L. Song, *J. Mater. Chem. A* **2015**, *3*, 9092-9097.

17   [43]   K. Cao, Z. Zuo, J. Cui, Y. Shen, T. Moehl, S. M. Zakeeruddin, M. Grätzel, M. Wang,

18   *Nano Energy* **2015**, *17*, 171-179.

19   [44]   Y. Jiang, M. R. Leyden, L. Qiu, S. Wang, L. K. Ono, Z. Wu, E. J. Juarez-Perez, Y. B.

20   Qi, *Adv. Funct. Mater.* **2018**, *28*, 1703835.

21   [45]   M. R. Leyden, Y. Jiang, Y. B. Qi, *J. Mater. Chem. A* **2016**, *4*, 13125-13132.

22   [46]   H. Chen, F. Ye, W. Tang, J. He, M. Yin, Y. Wang, F. Xie, E. Bi, X. Yang, M. Grätzel,

23   L. Han, *Nature* **2017**, *550*, 92-95.

24   [47]   Wikipedia. https://en.wikipedia.org/wiki/Chemical_vapor_deposition   (accessed

25   December, 2018).

[48] Poly plant project. https://www.polyplantproject.com/cvdreactors.html (accessed December, 2018)

[49] Kaneka Corporation. http://www.kaneka-solar.com/product/thin-film/pdf/U-EA.pdf (accessed December, 2018).

[50] Sono-Tek Corporation. http://www.sono-tek.com/thin-film-overview/ (accessed Febrary, 2018).

[51] N. Ahn, D. Y. Son, I. H. Jang, S. M. Kang, M. Choi, N. G. Park, *J. Am. Chem. Soc.* **2015**, *137*, 8696-8699.

[52] Y. Wu, A. Islam, X. Yang, C. Qin, J. Liu, K. Zhang, W. Peng, L. Han, *Energy Environ. Sci.* **2014**, *7*, 2934-2938.

[53] Wikipedia. https://en.wikipedia.org/wiki/Dimethylformamide (accessed December, 2018).

[54] Wikipedia. https://en.wikipedia.org/wiki/Dimethyl_sulfoxide (accessed December, 2018).

[55] J. Yin, H. Qu, J. Cao, H. Tai, J. Li, N. Zheng, *J. Mater. Chem. A* **2016**, *4*, 13203-13210.

[56] W. Qiu, T. Merckx, M. Jaysankar, C. M. Huerta, L. Rakocevic, W. Zhang, U. W. Paetzold, R. Gehlhaar, L. Froyen, J. Poortmans, D. Cheyns, H. J. Snaith, P. Heremans, *Energy Environ. Sci.*, **2016**, *9*, 484-489.

[57] Q. Jiang, L. Zhang, H. Wang, X. Yang, J. Meng, H. Liu, Z. Yin, J. Wu, X. Zhang, J. You, *Nat. Energy* **2016**, *2*, 16177.

[58] G. E. Eperon, S. D. Stranks, C. Menelaou, M. B. Johnston, L. M. Herz, H. J. Snaith, *Energy Environ. Sci.* **2014**, *7*, 982.

[59] J. W. Lee, D. J. Seol, A. N. Cho, N. G,Park, *Adv. Mater.* **2014**, *26*, 4991-4998.

[60] Q. Chen, H. Zhou, T. B. Song, S. Luo, Z. Hong, H. S. Duan, L. Dou, Y. Liu, Y. Yang, *Nano Lett*. **2014**, *14*, 4158-4163.

[61] Y. Zhao, K. Zhu, *J. Phys. Chem. C* **2014**, *118*, 9412-9418.

[62]   C. Mu, J. Pan, S. Feng, Q. Li, D. Xu, *Adv. Energy Mater.* **2017**, *7*, 1601297.

[63]   Wikipedia. https://en.wikipedia.org/wiki/Sputter_deposition (accessed December, 2018).

[64]   Kaivo Optoelectronic Technology Co. Ltd. http://www.zh-kv.com/Kaivo_En/ProductView.asp?ID=19&SortID=128 (accessed December, 2018).

[65]   J. E. Bishop, T. J. Routledge, D. G. Lidzey, *J. Phys. Chem. Lett.* **2018**, *9*, 1977-1984.

[66]   D. Abou-Ras, Rau, U. Thomas Kirchartz, *Second edition. Weinheim: Wiley-VCH-Verl* **2016**.

[67]   T. Kirchartz, U. Rau, M. Kurth, J. Mattheis, J. H. Werner, *Thin Solid Films* **2007**, *515*, 6238-6242.

[68]   K. Domanski, E. A. Alharbi, A. Hagfeldt, M. Grätzel, W. Tress, *Nat. Energy* **2018**, *3*, 61-67.

[69]   A. Tiihonen, K. Miettunen, J. Halme, S. Lepikko, A. Poskela, P. D. Lund, *Energy Environ. Sci.* **2018**, *11*, 730-738.

[70]   N. Yaghoobi Nia, M. Zendehdel, L. Cinà, F. Matteocci, A. Di Carlo, *J. Mater. Chem. A* **2018**, *6*, 659-671.

[71]   A. Dualeh, P. Gao, S. I. Seok, M. K. Nazeeruddin, M. Grätzel, *Chem. Mater.* **2014**, *26*, 6160-6164.

[72]   E. J. Juarez-Perez, Z. Hawash, S. R. Raga, L. K. Ono, Y. B. Qi, *Energy Environ. Sci.* **2016**, *9*, 3406-3410.

[73]   E. J. Juarez-Perez, L. K. Ono, M. Maeda, Y. Jiang, Z. Hawash, Y. B. Qi, *J. Mater. Chem. A* **2018**, *6*, 9604-9612.

[74]   J. A. Christians, P. A. Miranda Herrera, P. V. Kamat, *J. Am. Chem. Soc.* **2015**, *137*, 1530-1508.

[75]   N. Aristidou, C. Eames, I. Sanchez-Molina, X. Bu, J. Kosco, M. S. Islam, S. A. Haque, *Nat. Commun.* **2017**, *8*, 15218.

1   [76]   A. K. Jena, M. Ikegami, T. Miyasaka, *ACS Energy Lett.* **2017**, *2*, 1760-1761.

2   [77]   Y. Zhao, W. Zhou, H. Tan, R. u, Q. Li, F. Lin, D. Yu, G. Walters, E. H. Sargent, Q.

3   Zhao, *J. Phys. Chem. C* **2017**, *121*, 14517-14523.

4   [78]   Y. Yuan, J. Huang, *Acc. Chem. Res.* **2016**, *49*, 286-293.

5   [79]   K. Domanski, J. P. Correa-Baena, N. Mine, M. K. Nazeeruddin, A. Abate, M. Saliba,

6   W. Tress, A. Hagfeldt, M. Grätzel, *ACS Nano* **2016**, *10*, 6306-6314.

7   [80]   J. Ávila, C. Momblona, P. P. Boix, M. Sessolo, H. J. Bolink, *Joule* **2017**, *1*, 431-442.

8   [81]   J. A. Christians, P. Schulz, J. S. Tinkham, T. H. Schloemer, S. P. Harvey, B. J. Tremolet

9   de Villers, A. Sellinger, J. J. Berry, J. M. Luther, *Nat. Energy* **2018**, *3*, 68-74.

1
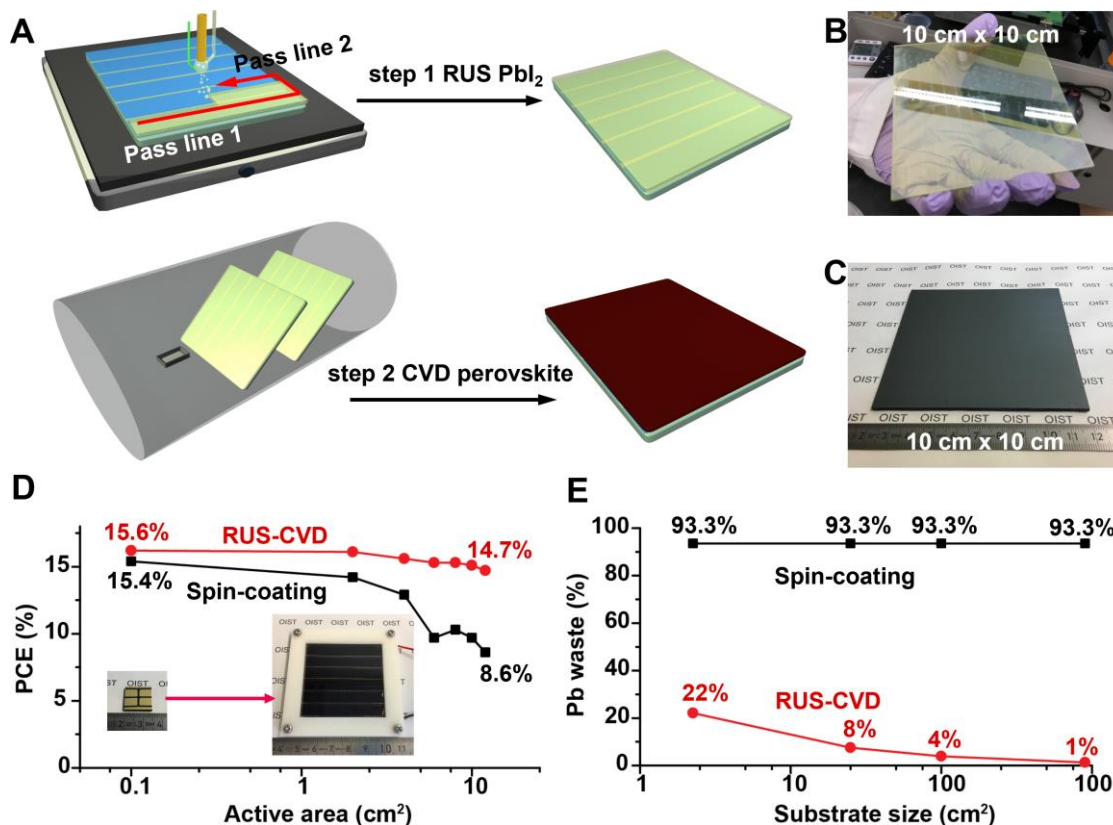
2

3 **Figure 1.** Perovskite film deposition. (A) Schematic drawing of the RUS-CVD perovskite film
4 deposition technology. PbI_2 films are raster ultrasonic spray (RUS)-coated on the FTO/ compact
5 TiO_2 (c-TiO_2) substrates, and converted to $FAPbI_xBr_{3-x}$ via a CVD process. Photograph of (B)
6 a RUS-coated PbI_2 film before annealing and (C) a CVD converted $FAPbI_xBr_{3-x}$ film deposited
7 on a 10 cm × 10 cm patterned FTO substrate. (D) Solar cell and module performance as a
8 function of active area. Spin-coating data are extracted from our previous work.[44] The RUS-
9 CVD method shows much lower substrate size dependence than the spin-coating method. (E)
10 Lead waste during the perovskite deposition process as a function of substrate size. Lead waste
11 during the RUS-CVD process continuously decreases until negligible, much less than that
12 generated during the spin-coating process.

13
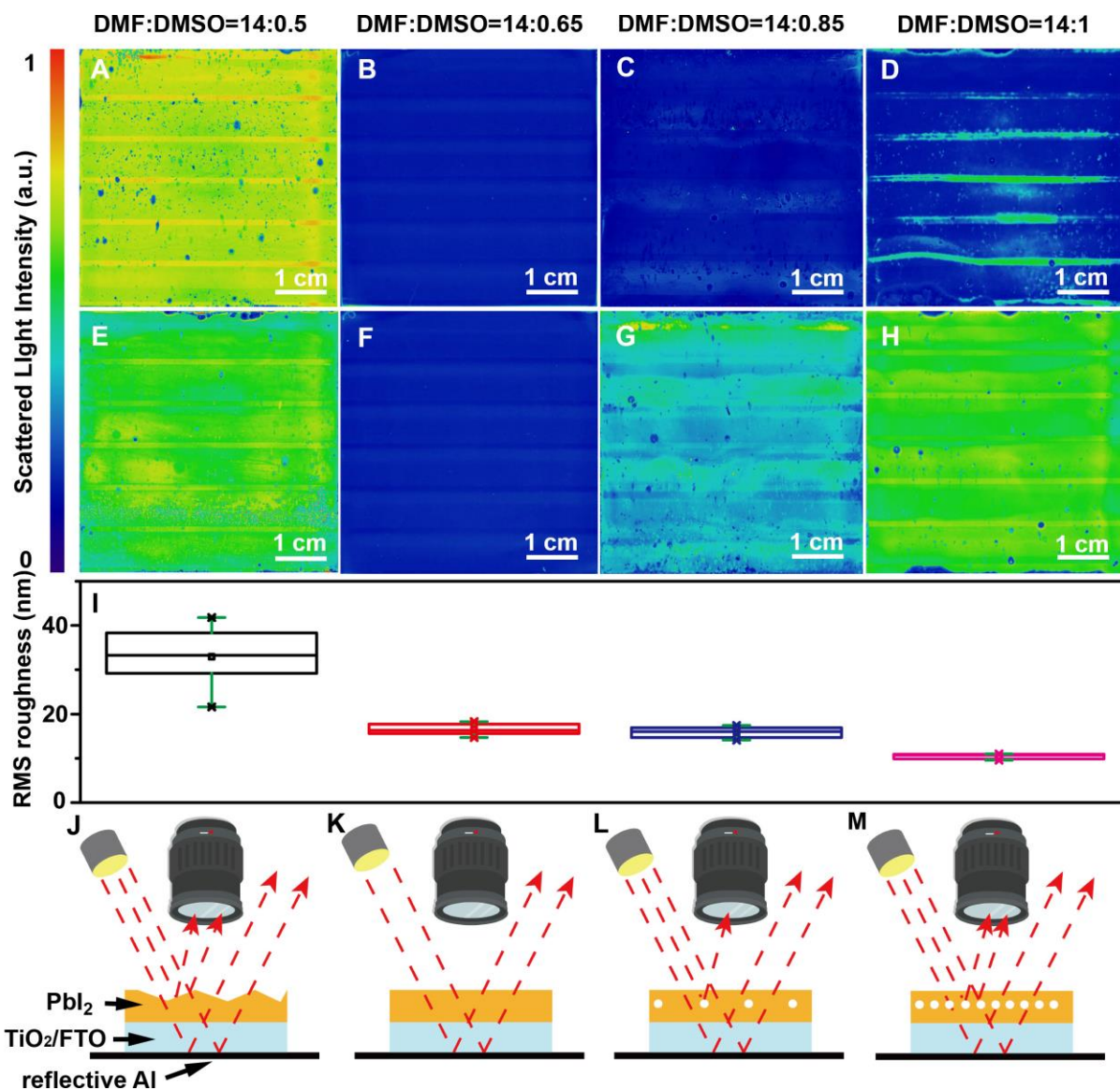
Figure 2. Effect of solvent mixture on the PbI_2 film texture. False-color monochrome scattered light optical images of (A-D) PbI_2 precursor films after spray-coating (solvent allowed to evaporate at process temperature) (E-H) PbI_2 precursor films after annealing to remove the coordinated DMSO. Optical images show the entire 5 cm × 5 cm substrates. (I) Root mean square (RMS) roughness of spray-coated PbI_2 films. AFM measurements are performed on 6 positions of each 5 cm × 5 cm substrate for statistical analysis. The DMF : DMSO ratios are 14:0.5 for 2A, 2E; 14:0.65 for 2B, 2F; 14:0.85 for 2C, 2G and 14:1 for 2D, 2H, respectively. (J-M) Schematic drawing showing the SLI mapping measurements on the different PbI_2 films. Increasing the DMSO ratio results in reduced film surface roughness but increased internal cracks and voids.
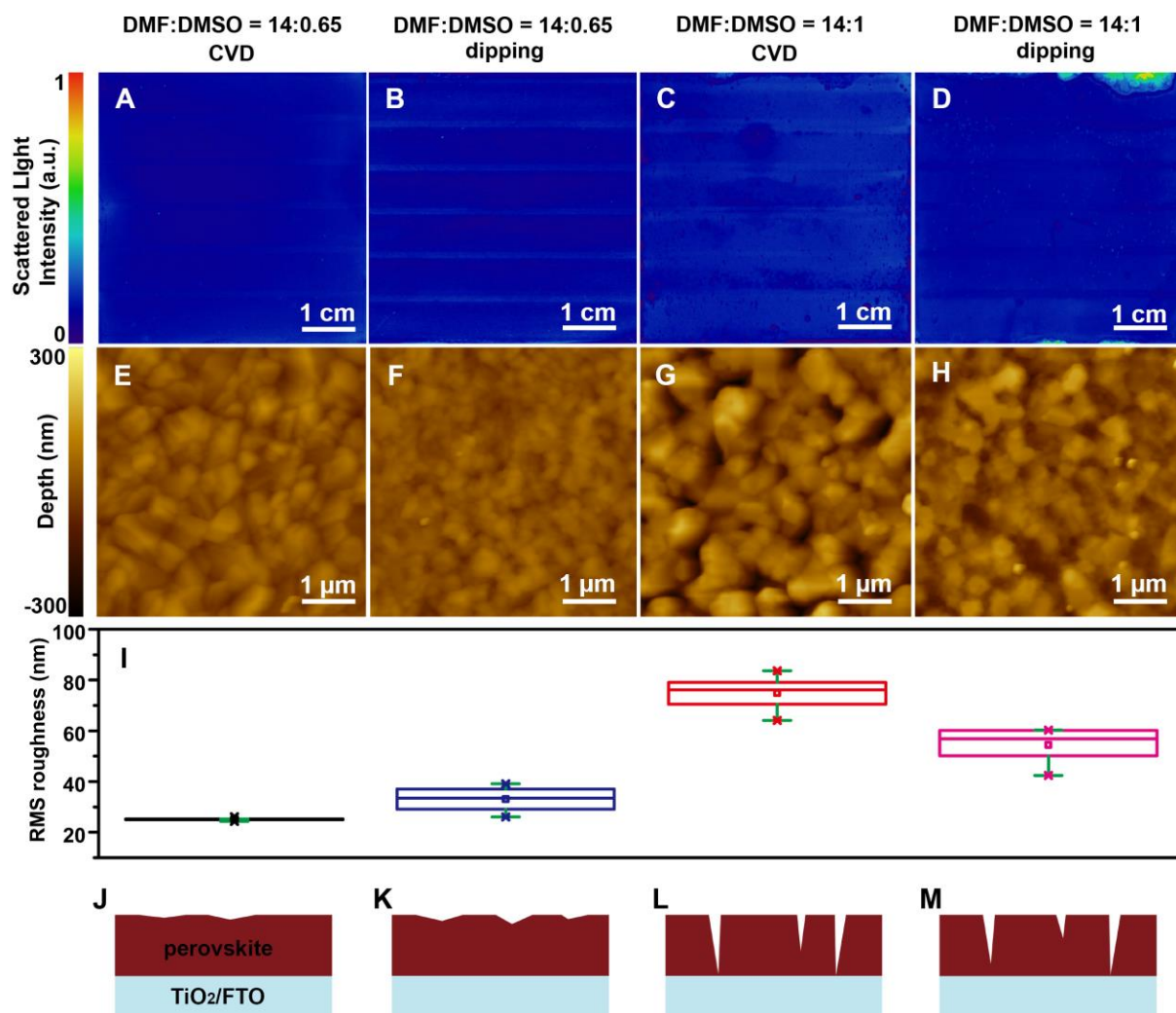
Figure 3. Perovskite film morphology. (A-D) False-color monochrome scattered light optical images of perovskite films. (E-H) AFM morphology of perovskite films. (I) Root mean square (RMS) roughness of the $FAPb(I_xBr_{1-x})_3$ films. AFM measurements are performed on 6 positions of each 5 cm × 5 cm substrate for statistical analysis. (J-M) Schematic drawing showing the characteristics of the $FAPb(I_xBr_{1-x})_3$ films converted by CVD and the dipping (D) process. The perovskite films are prepared by (A, E) RUS (DMF : DMSO = 14 : 0.65)-CVD, (B, F) RUS (DMF : DMSO = 14 : 1)-CVD, (C, G) RUS (DMF : DMSO = 14 : 0.65)-D, (D, H) RUS (DMF : DMSO = 14 : 1)-D, respectively. Perovskite films converted using RUS (DMF : DMSO = 14 : 0.65) PbI_2 show high uniformity without pin-holes.
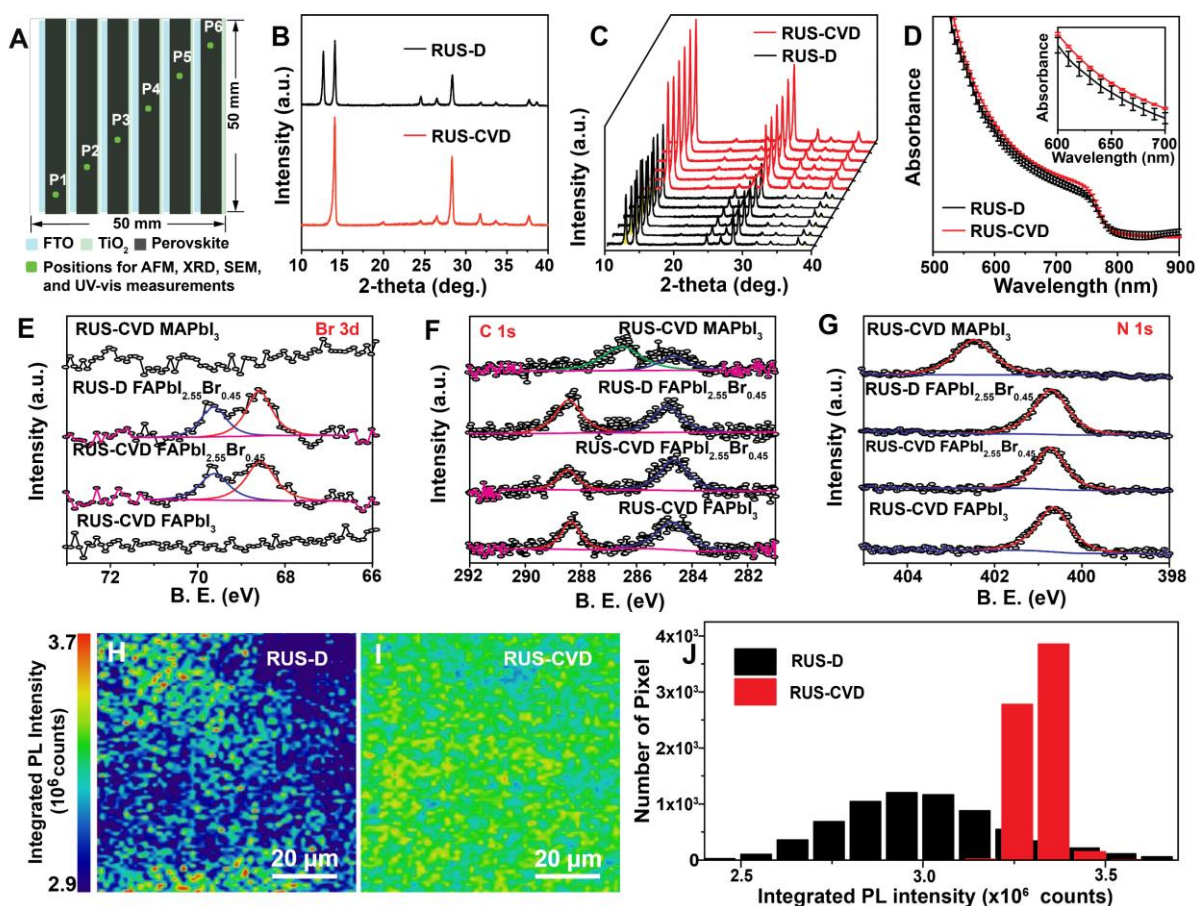
Figure 4. Perovskite film composition and optical property. (A) Schematic drawing showing the 6 positions for the AFM, SEM, XRD, and UV-Vis measurements. (B-C) XRD pattern, (D) UV-Vis absorbance spectra of $FAPb(I_{0.85}Br_{0.15})_3$ perovskite films. (E) Br 3d, (F) C 1s and (G) N 1s HRXPS spectra on $FAPb(I_{0.85}Br_{0.15})_3$ perovskite films. (H-I) false-color monochrome PL mapping images of the $FAPb(I_{0.85}Br_{0.15})_3$ films. (J) PL intensity histogram extracted from Figure 4H-I. Perovskite films converted by CVD and dipping have the similar composition of $FAPb(I_{0.85}Br_{0.15})_3$. The Perovskite films converted by CVD show complete conversion with higher perovskite crystallinity, absorbance and PL intensity than the dipping converted perovskite films.
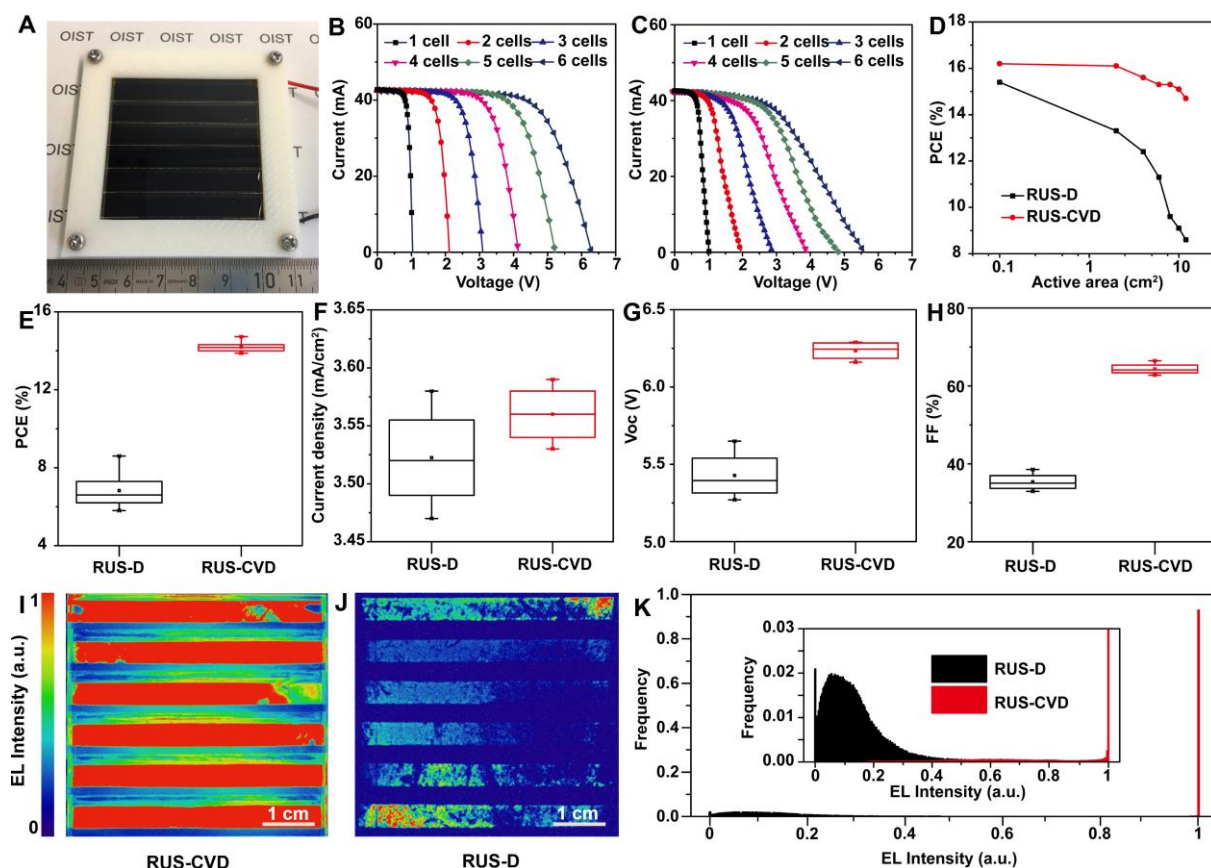
Figure 5. Perovskite solar module performance. (A) Photograph of a 5 cm × 5 cm FAPb(I$_{0.85}$Br$_{0.15}$)$_3$ perovskite module. (B-C) J-V curves of the champion perovskite modules prepared by (B) RUS-CVD and (C) RUS-D method. (D) Solar cell and module performance as a function of active area. The RUS-CVD method shows higher module performance and lower substrate-size dependence than the RUS-D method. Statistical results of the module (E) PCE, (F) current density, (G) V$_{oc}$ and (H) fill factor. A total of 16 modules (8 modules prepared by RUS-CVD and 8 modules prepared by RUS-D) are prepared for the statistical analysis. The RUS-CVD prepared modules show higher performance than the RUS-D prepared modules because of slightly higher Jsc and significantly higher Voc and FF. False-color monochrome EL mapping images of perovskite modules prepared by (I) RUS-CVD and (J) RUS-D methods. (K) EL intensity histogram extracted from Figure 5I-J. The inset is the histogram with low maximum frequency in Y axis. The RUS-CVD prepared module shows higher EL intensity, suggesting the RUS-CVD prepared perovskite has much less non-radiative recombination centers.
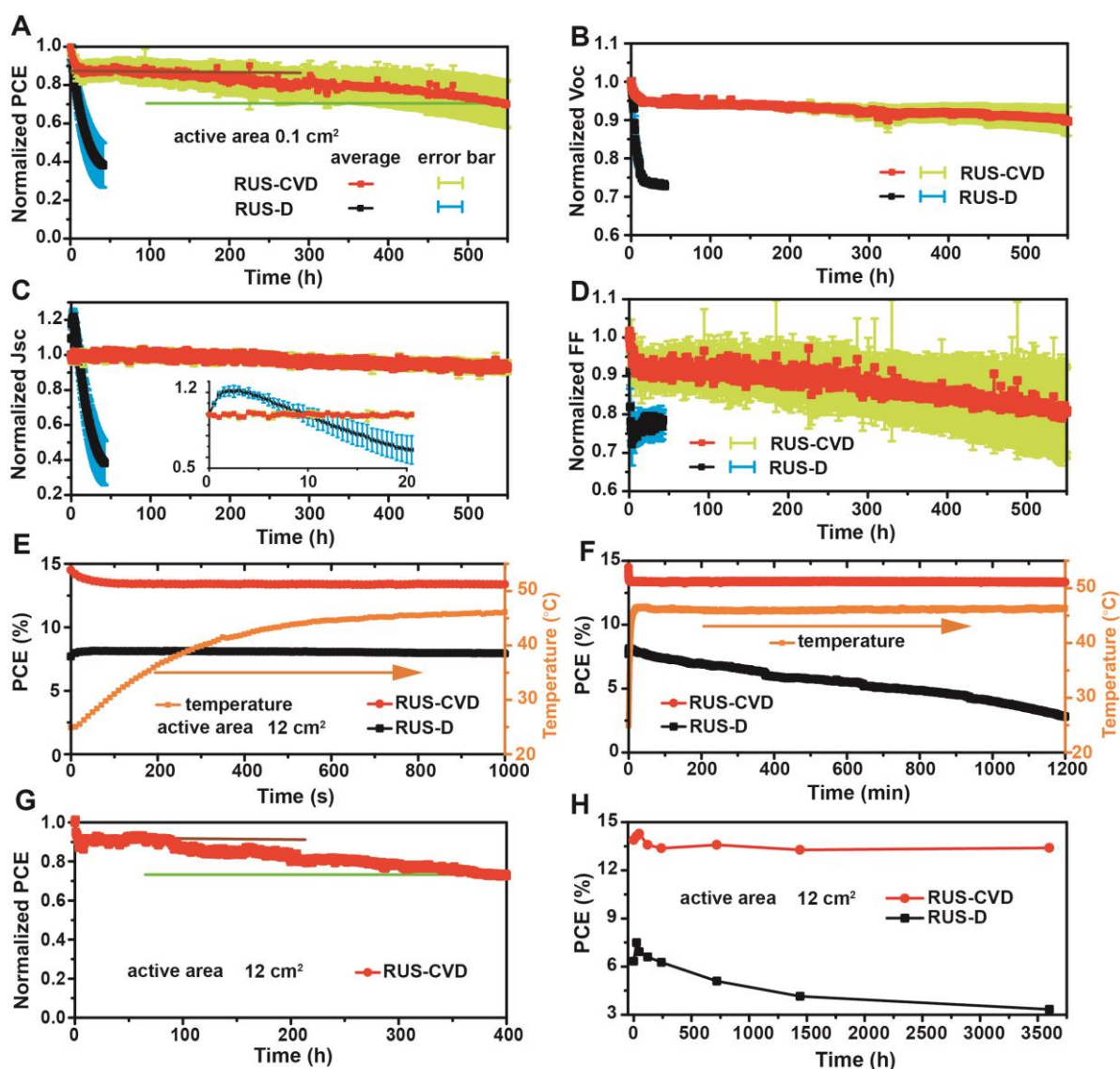
Figure 6. Stability of the perovskite solar cells and module. (A) Normalized average efficiency, (B) V_{oc}, (C) J_{sc} and (D) FF obtained on 4 unencapsulated perovskite solar cells (active area = 0.1 cm^2). Devices are kept at 1 sun, N$_2$ atmosphere (<5% relative humidity), at their maximum power point and measured by step J-V scans every 30 min. The inset of (C) is the enlarged region of (C) between 0-20 h. Jsc of the RUS-D samples increases in the first 2 h until reach the maximum value and then decreases. (E-F) Steady-state maximum power output (Vmpp of 4.50 V for RUS-CVD and 3.10 V for RUS-D) of the champion perovskite modules (active area = 12 cm^2). Measurements are performed at 1 Sun, MPP condition, N$_2$ atmosphere, <5% relative humidity and without encapsulation. (G) Normalized efficiency obtained on a RUS-CVD prepared perovskite module under the MPP condition. (H) Storage stability of the perovskite solar modules. Modules are stored in dark, N$_2$ atmosphere. For the RUS-CVD sample (Figure 6A, 6G), the brown line indicates the starting point of the linear region and the green line shows the time when PCE decays to 80% with respect to the starting point. The perovskite solar cells/module prepared by RUS-CVD show higher operational and storage stability.
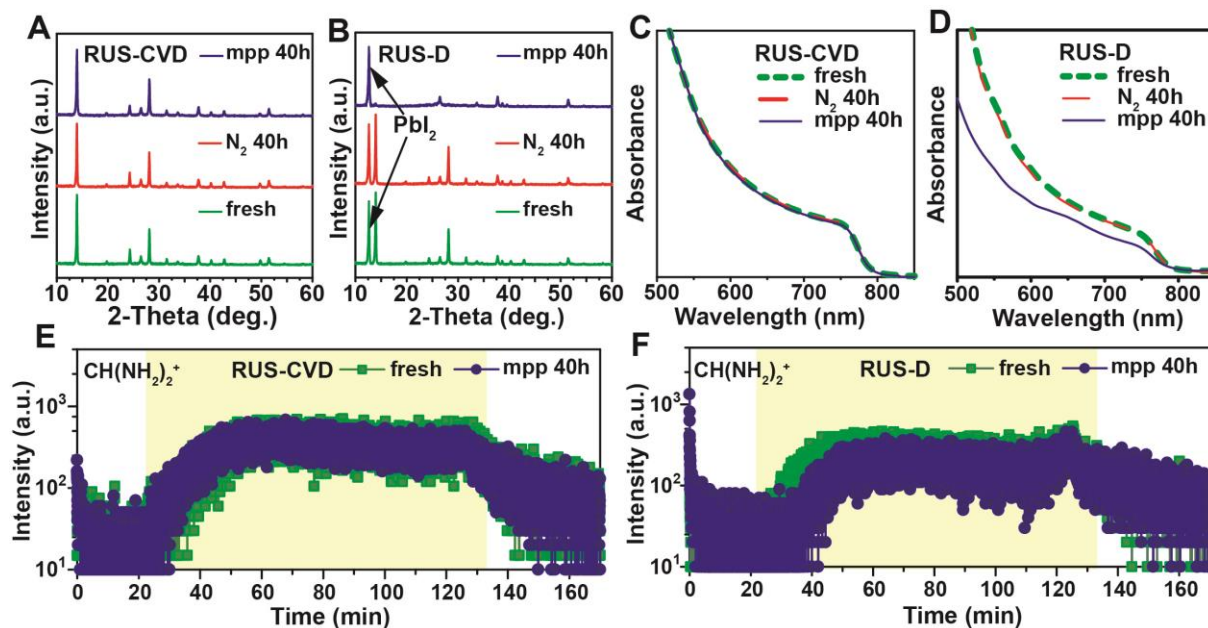
Figure 7. Effect of perovskite deposition methods on device operational stability. (A-B) XRD patterns and (C-D) UV-vis absorbance spectra of fresh, storage and operated devices. Gold electrodes are removed before measurements. Under the same operational condition (mpp 40 h), the RUS-CVD sample do not decompose but the RUS-D sample decomposes significantly. (E-F) SIMS depth profile of FA$^+$ upon degradation. Measurements are taken on the fresh and operated devices that prepared by (E) RUS-CVD and (F) RUS-D. Under the same operational condition (mpp 40 h), the RUS-CVD sample does not show FA$^+$ ion migration but the RUS-D sample shows obvious ion migration from the perovskite film surface to bulk. Different perovskite film decomposition and FA$^+$ ion migration behavior result in different device operational stability.
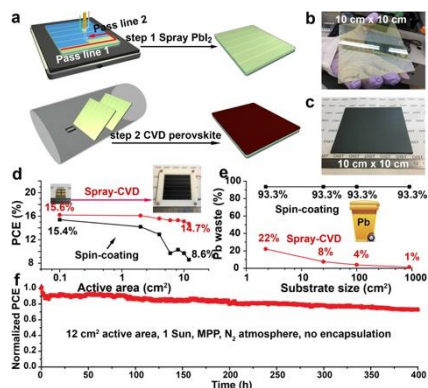
1 **A negligible-Pb-waste and upscalable perovskite film processing method** combining raster
2 ultrasonic spray coating and chemical vapor deposition is developed. Planar-structured
3 perovskite solar module shows a PCE of 14.7% on an active area of 12 cm^2, much lower
4 substrate-size dependence than the spin-coating method, and outstanding operational stability
5 near the maximum power point under 1 Sun light illumination (T$_{80}$ lifetime of 388 h).

6
7 **Keyword:** perovskite, solar module, upscalable, Lead waste, stability
8
9
10 Yan Jiang, Mikas Remeika, Zhanhao Hu, Emilio J. Juarez-Perez, Longbin Qiu, Zonghao Liu,
11 Taehoon Kim, Luis K. Ono, Dae-Yong Son, Zafer Hawash, Matthew R. Leyden, Zhifang Wu,
12 Lingqiang Meng, Jinsong Hu, and Yabing Qi*
13
14
15 **Negligible-Pb-Waste and Upscalable Perovskite Deposition Technology for High**
16 **Operational-Stability Perovskite Solar Modules**
17
18 ToC figure
19

20
21